Photochemical & Photobiological Sciences

PAPER

Cite this: *Photochem. Photobiol. Sci.*, 2019, **18**, 2469

Unraveling the photocatalytic properties of TiO_2/WO_3 mixed oxides†

Leonardo F. Paula,‡[a] Moritz Hofer,‡[b] Veronica P. B. Lacerda,[a] Detlef W. Bahnemann[b,c] and Antonio Otavio T. Patrocinio *[a]

Received 5th April 2019,
Accepted 27th July 2019

DOI: 10.1039/c9pp00163h

rsc.li/pps

TiO_2/WO_3 heterojunctions are one of the most investigated systems for photocatalytic applications. However, distinct behavior can be found in the literature depending on the pollutant to be degraded and the photocatalyst preparation conditions. Some authors reported improved photocatalytic activities in relation to TiO_2, while others a deleterious effect. Different factors have been identified to influence the activity of such systems. In this work, a systematic investigation of TiO_2/WO_3 samples with different W/Ti ratios (0–100%) was carried out using different pollutants as targets (gaseous NO, acetaldehyde and aqueous methylene blue solutions). A detailed structural investigation along with transient absorption studies and photoelectrochemical measurements allowed the rationalization of some of the previously reported factors that control the TiO_2/WO_3 photoactivity, *i.e.* the inability to reduce molecular oxygen, the stabilization of the anatase phase and the adsorption surface properties. The investigations also identified a factor not previously reported: in TiO_2/WO_3 systems, a fraction of long-lived holes do not take part in the interfacial charge transfer to efficient hole quenchers, such as methanol. This behavior seems to be related to the doping of the TiO_2 matrix with W(VI) and plays a key role in the photocatalytic activity.

Introduction

The formation of type II heterojunctions between TiO_2 and a second semiconductor with smaller conduction band energy levels is one of the most common strategies to develop improved TiO_2-based photocatalysts for different applications.[1–4] In this strategy, an enhancement in the electron–hole lifetimes in relation to those of bare TiO_2 is expected, as the photogenerated electrons are trapped in the material with the smallest conduction band energy while the holes are transferred to TiO_2. Moreover, an extension of the light absorption range towards the visible region of the spectrum is typically observed.

A myriad of materials have been coupled to TiO_2 to yield heterojunctions, but the heterojunction formed by TiO_2 and WO_3 calls particular attention (Scheme 1). WO_3 has a smaller band gap than TiO_2 due to its more positive conduction band edge. As a result, WO_3 acts as an electron sink, improving the charge separation efficiency. Different strategies have been employed to produce TiO_2/WO_3 heterojunctions in which the optimal WO_3 content varies between 1 and 4 mol%.[5–21] In the literature, controversial reports can be found when degradation of different pollutants is analyzed. Some authors reported improved photocatalytic activities for TiO_2/WO_3 in relation to TiO_2,[8,11,18,22,23] while others described a deleterious effect related to the addition of WO_3 to the photocatalyst.[24–26] J. Yang *et al.*[27] observed that the influence of WO_3 on the photocatalytic activity of TiO_2 is complicated and should be related to the crystal phase, the electron accumulation ability of WO_3 and the degradation mechanism of pollutants. Electron transfer from TiO_2 to the WO_3 conduction band inhi-

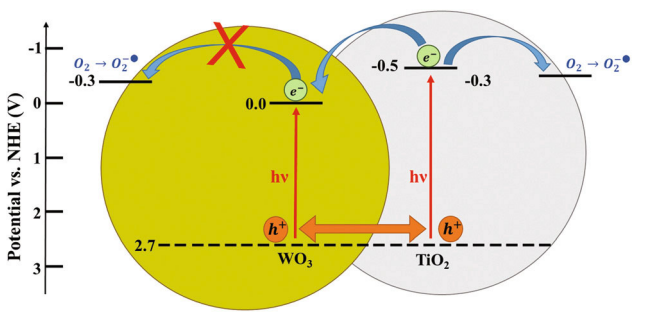

Scheme 1 Energy levels in type II TiO_2/WO_3 heterojunctions.

[a]*Laboratory of Photochemistry and Materials Science, Institute of Chemistry, Federal University of Uberlandia, Brazil. E-mail: otaviopatrocinio@ufu.br*
[b]*Institute of Technical Chemistry, Leibniz University Hannover, Hannover, Germany*
[c]*Laboratory "Photoactive Nanocomposite Materials", Saint-Petersburg State University, Saint-Petersburg, Russia*

†Electronic supplementary information (ESI) available. See DOI: 10.1039/c9pp00163h

‡Both authors contributed equally to this work.

bits the one electron reduction of molecular oxygen, leading to the observation of photochromism after UV irradiation.

Further, L. Yang and co-workers[28] have investigated the role of amorphous WO_x species on the surface of TiO_2 which influences both the surface acidity and the electronic properties. More recently, Žerjav *et al.* have used time-resolved infrared spectroscopy to identify shallow and deep electron trapping states in TiO_2/WO_3 mixtures which were correlated with photocatalytic performance towards bisphenol oxidation.[29] So far, it is not clear how all these factors can be controlled by varying the preparation conditions and how differently they affect the degradation of different pollutants.

Aiming at the rationalization of the main factors that influence the photocatalytic performance of TiO_2/WO_3 photocatalysts, in this work a systematic investigation of TiO_2/WO_3-based photocatalysts was performed. Samples with different W/Ti molar ratios varying from 0 to 100% were prepared and fully characterized, and their activities towards oxidative photodegradation of gaseous and aqueous pollutants were investigated. These data were correlated with ns-transient absorption spectroscopy and photoelectrochemical measurements, allowing the establishment of the main factors that affect the photocatalytic activity of these materials.

Experimental

Preparation of the TiO_2/WO_3 photocatalysts

All reactants and solvents were of analytical and HPLC grade, respectively. $Na_2WO_4{\cdot}2H_2O$, titanium(IV) isopropoxide (TTIP), ethyl cellulose (45 CP), terpineol and potassium sulfate were acquired from Sigma-Aldrich and used as received. Deionized water (18.2 MΩ cm^{-1}) was used in all experiments.

Pure WO_3 and TiO_2 photocatalysts as well as W–Ti mixed oxides (WT) were prepared by the hydrothermal sol–gel method. Pure WO_3 was prepared by dissolving $Na_2WO_4{\cdot}2H_2O$ in a minimum amount of deionized water, which was passed through a cation exchange resin (Sigma-Aldrich, Dowex 50 WX2 hydrogen form, 100–200 mesh) to replace Na^+ by H^+. The so-obtained greenish H_2WO_4 solution was heated at 80 °C for 4 h under vigorous stirring to accelerate the hydrolysis. After aging overnight under magnetic stirring at room temperature, the gel was loaded in a Teflon-lined autoclave and heated at 200 °C for 8 h (180 psi). Afterwards, the solid was centrifuged and dried in an oven at 70 °C. The yellow powder was manually ground and finally calcined in air at 500 °C for 2 h.

Bare TiO_2 was prepared as reported previously.[30,31] Briefly, 12 ml of TTIP were added dropwise to 70 ml of 0.1 M HNO_3 solution. The sol was then aged at 80° C for 8 h and submitted to the same hydrothermal and thermal treatment described for bare WO_3. The W–Ti mixed oxides were produced by adding dropwise the required amount of TTIP to the H_2WO_4 solutions under vigorous stirring in order to obtain nominal molar W/Ti ratios of 1 : 80, 1 : 40, 1 : 20, 1 : 10, 1 : 5, 1 : 4, 1 : 3, 1 : 2 and 1 : 1, labeled as WT80, WT40, WT20, WT10, WT5, WT4, WT3, WT2 and WT1, respectively. Afterwards, the suspensions were aged and hydrothermally and thermally treated as the bare oxides.

Characterization

Electronic absorption spectra were recorded on a double beam Shimadzu UV-1650 spectrophotometer or a Cary 100 UV–Vis spectrophotometer (Varian) equipped with an integration sphere for diffuse reflectance measurements. Attenuated total reflectance Fourier-transform infrared (ATR-FTIR) spectra were recorded using a PerkinElmer Frontier spectrometer. The measurements were performed on a diamond crystal plate, using 32 scans at a resolution of 2 cm^{-1}. X-ray diffractograms of the powders were obtained using a Shimadzu XRD-6000 diffractometer, with a CuKα (λ = 1.54148 nm) monochromatic source or a D8 Advance diffractometer (Bruker) operating with CuKα 1,2 as the radiation source. The scans were recorded over an angular range of 5–110° 2θ with a step width of 0.013° 2θ and a step time of 0.7 s, measuring in $\theta/2\theta$ geometry. Rietveld refinements of the XRD data were performed using TOPAS software. Crystallite sizes were calculated based on the peak widths assuming Lorentzian shaped peaks. Lattice parameters were determined according to the positions of the reflections using Crystallographic Information Files (CIF). The corresponding errors were also calculated by TOPAS.

Specific surface area measurements were determined from N_2 adsorption/desorption isotherms using the BET methodology[32] and a Quantachrome NOVAtouch LX1 surface analyzer. X-ray photoelectron spectroscopy (XPS) was carried out employing a Leybold Heraeus analyser equipped with an Al non monochromatic X-ray source and a hemispherical electron energy analyzer. The beam energy was 1484 eV, and the residual C 1s peak at 284.6 eV was used as the internal standard.

Field emission scanning electron microscopy (FESEM) images were obtained using a Jeol JSM 6700F microscope at 2.0 kV acceleration voltage. Transmission electron microscopy (TEM) images were acquired using a Tecnai G2 F20 TMP microscope (FEI Company) at 200 kV accelerating voltage. Raman spectra were collected using a LabRAM HR Evolution confocal microscope. Samples were excited at 532 nm, and the presented spectra were obtained by the accumulation of 8 scans in the range of 70 to 2000 cm^{-1}.

Transient absorption spectroscopy (TAS) was carried out employing a LKS80 nanosecond laser flash photolysis spectrometer (Applied Photophysics) equipped with the appropriate diffuse reflectance accessory as described previously.[33] The samples were placed in a closed quartz cuvette, purged with N_2 and excited with a 355 nm laser beam (3.0 mJ cm^{-2} per pulse). The pump beam was produced by a Nd:YAG laser (Quantel; Brilliant B; third harmonic, 355 nm). The transient signals were collected by a PMT (Hammatsu R928) connected to a DSO9064A oscilloscope (Agilent). The transient decay is presented as the variation in the reflectance (ΔJ), which is calculated according to eqn (1),[34] where I_0 is the incident intensity of the analyzing light; J_0 is the diffuse reflected light without laser pulse (ground light level); and J_x is the diffuse reflected light with the laser pulse. It has been reported that the ΔJ

value can be correlated with the transient absorption provided that ΔJ is less than 0.3;[35,36] thus, to describe the results obtained by the detection of the diffuse reflected light, the term transient absorption will be used here.

$$\Delta J = \frac{J_0/I_0 - J_x/I_0}{J_0/I_0} = \frac{J_0 - J_x}{J_0} \quad (1)$$

Photoelectrochemical characterization of the mixed oxides was carried out by preparing thin films of the different powders by the screen printing technique.[31] The as prepared films were then submitted to calcination at 450 °C for 4 h in order to ensure mechanical stability. Photoelectrochemical experiments were carried out in a Zennium potentiostat and a PECC-2 photoelectrochemical cell (Zahner-Elektrik GmbH & Co. KG). A Pt wire was used as the counter electrode along with a Ag/AgCl, NaCl 3 mol L^{-1} reference electrode. A 6.5 pH K_2SO_4 0.1 mol L^{-1} solution was employed as the electrolyte. 10% (v/v) of methanol was also added to the electrolyte in some experiments. Samples were illuminated using a LOT solar simulator equipped with a 300 W Xe lamp and an A.M. 1.5 filter. The light intensity was adjusted to 100 mW cm^{-2}. All reported potentials are against NHE (−0.209 mV *vs.* Ag/AgCl, NaCl 3 mol L^{-1}). Electrochemical impedance spectroscopy (EIS) was carried out under illumination in the frequency range of 1 MHz–100 mHz and at +1 V *vs.* NHE. 0.1 mol L^{-1} K_2SO_4 solution was used as the electrolyte. The experiments were performed at pH = 5.7.

Photocatalytic properties

The photocatalytic activities of the as prepared samples were measured towards different targets. Acetaldehyde and NO gas phase degradation was carried out following the ISO 22197-2 and 22197-1 standards, respectively.[37,38] For acetaldehyde degradation, the experiments were carried out under UV (365 nm; 1 mW cm^{-2}) and visible (425 nm; 3 mW cm^{-2}) irradiation. The sample surfaces were exposed to a 1 L s^{-1} gas flow having ~1 ppm of acetaldehyde in air at 50% relative humidity. Variations in acetaldehyde concentration were measured every 5 minutes using a Syntech 955 gas chromatograph. Similar conditions were employed for NO degradation; however, the gas flow was 3 L s^{-1}. The concentrations of NO and NO_x along the time were determined using a Teledyne API T200 chemiluminescence NO/NO_x analyzer. Some experiments were also carried out under anaerobic conditions by replacing the carrier gas with pure N_2.

Aqueous methylene blue (MB) degradation was carried out in a borosilicate reactor at 25 °C, following the ISO 10678 standards.[39,40] The initial MB concentration was 2×10^{-5} mol L^{-1}, and 0.1 g L^{-1} of the photocatalyst were loaded in each experiment. After 60 minutes under stirring in the dark, the suspension was exposed to a 300 W Xe lamp equipped with a KG1 filter to eliminate UV-B and UV-C photons. The light intensity was determined using a radiometer (PMA2100 Solar Light Co). For all assays, the photocatalytic activity is presented in terms of photonic efficiency (ξ), eqn (2), in which r is the rate of product formation or reagent disappearance and I is the light intensity.

$$\xi = \frac{r}{I} \times 100 \quad (2)$$

Results

Structural and electronic characterization

Bare TiO_2, obtained by the sol–gel method followed by hydrothermal treatment, is constituted mainly by anatase nanocrystals, as previously described[31] and confirmed by XRD analysis (Fig. 1). In addition to the anatase peaks, rutile (ICDD 01-089-0552) and brookite (ICDD 01-076-1934) phases were identified, as revealed by the (1 0 0) reflection at 2θ = 27.2° and the (2 1 1) reflection at 2θ = 30.6°, respectively. The bare WO_3 exhibits sharper and more intense diffraction peaks which indicated larger crystallites with higher crystallinity in relation to TiO_2. It is constituted solely by the monoclinic (ICDD 01-072-1465) phase and is hereafter referred to as m-WO_3.

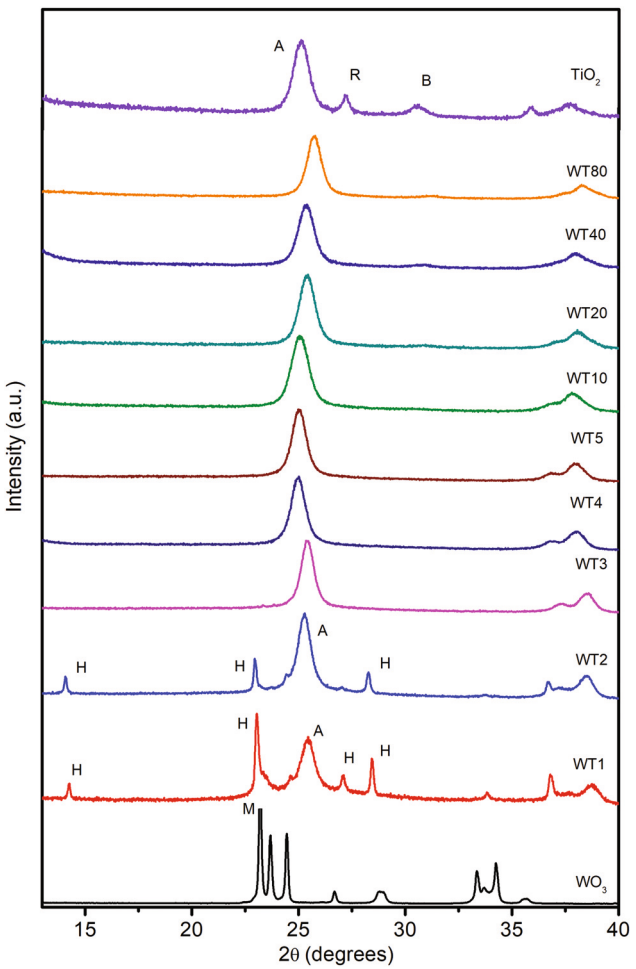

Fig. 1 X-ray diffractograms of bare TiO_2, WO_3 and WT samples with different W(VI)/Ti(IV) molar ratios. A denotes anatase, R rutile, B brookite, H hexagonal and M monoclinic.

The hydrolysis of TTIP in the presence of H_2WO_4 should lead to mixed and well interconnected TiO_2 and WO_3 particles, which is beneficial for photocatalysis due to the formation of heterojunctions between the two semiconductors. As the W(VI)/Ti(IV) molar ratio is varied, XRD analysis reveals that anatase is the main crystallographic phase under all conditions with shifted peak positions in relation to those for bare TiO_2. Interestingly, the shifts showed no systematics as a function of the W(VI) amount. No evidence for rutile was found upon addition of W(VI), which is in agreement with the data reported by Riboni *et al.*[41] for sol–gel prepared TiO_2/WO_3 samples with a different W(VI) precursor. The authors observed that the presence of W(VI) ions stabilizes the anatase phase, even when the samples are subjected to 700 °C. For the samples prepared here, no sign of rutile was observed up to 800 °C thermal treatment (Fig. S1, ESI†). Anatase is a metastable phase and transforms irreversibly to the most thermodynamically stable rutile phase at temperatures above 600 °C, when only TiO_2 is present. The transformation is known to be a nucleation and growth process. The crystallites have to grow to a critical nuclei size before the transformation can proceed.[42] The addition of W(VI) ions resulted in smaller anatase crystallite sizes, implying that W(VI) ions hindered the crystal growth of TiO_2 and thus the critical nuclei size could not be reached.[43] Moreover, the determination of the specific surface area (SSA) by N_2 adsorption/desorption isotherms (Fig. S2, ESI†) confirms that samples with low W(VI) loadings exhibit higher surface areas than bare TiO_2 (Table 1). This is likely due to the absence of larger rutile crystallites. With the exception of bare WO_3, all powders are mesoporous and exhibit type IV isotherms and H2-like hysteresis, indicating a large variation in the pore sizes. For bare WO_3, a type III isotherm was observed, which is characteristic of non-porous materials. The SSA of WO_3 is very low in relation to bare TiO_2, as shown in Table 1. The mixed oxides having up to 20 mol% W(VI) exhibit higher SSA than bare TiO_2. The SSA of WT3 is experimentally similar to that of TiO_2, and after this point, the values steadily decrease.

No reflections from crystalline WO_3 or any other W(VI) phase were observed in the XRD patterns of the samples with WO_3/TiO_2 molar ratios <1 : 2. These samples exhibit only anatase diffraction peaks. Reflections of hexagonal WO_3 (ICDD 01-075-2187, hereafter h-WO_3) could be found for the composites WT2 and WT1 with a nominal WO_3 content of 33.3 and 50 mol%, respectively.

Rietveld refinement was performed to evaluate the crystallite sizes and lattice parameters of the anatase phase as a function of the W(VI) content, as shown in Table 1. In pure TiO_2, the mean crystallite size of anatase was 14 nm, while rutile and brookite exhibit sizes of 37 and 11 nm, respectively. Anatase was slightly smaller in all composites, but, although the composite with the highest W(VI) amount (WT1) showed the smallest crystallite size, there was no continuous decrease with increasing W(VI) content. The crystallite size and cell parameters were also calculated for the WO_3 phases. In the specific case of WT1, h-WO_3 had a mean crystallite size of 45 nm and a and c parameters of 7.3097 and 7.7961 Å, respectively. Bare WO_3 (m-WO_3) showed much larger crystallites with an average size of 134 nm.

The lattice parameters of anatase were a = 3.7897 Å and c = 9.4925 Å in the pure TiO_2 sample, which differed from those of bulk anatase.[44] Changes of these parameters were observed as the W(VI) concentration was increased. The values were almost constant at low W(VI)/TI(IV) ratios. The a axis started to increase monotonously from WT40, while the c axis changed in the opposite direction (Fig. 2a). Moreover, the resulting unit cell volume increased from WT40 with increasing W(VI) amount, as shown in Fig. 2b

Changes in the lattice parameters of anatase due to the presence of W(VI) ions likely occur due to the substitution of Ti(IV) by W(VI) ions. These cations have similar ionic radii in an octahedral environment (0.0605 nm for Ti(IV) and 0.0600 nm for W(VI)), so it is expected that the latter can be introduced into the TiO_2 lattice.[45,46] Due to the higher ionic charge of W(VI), charge balancing had to be ensured. This could be accommodated in several ways. One was the appearance of interstitial O^{2-}, which is unlikely in TiO_2 lattices.[47] A more energetically favorable possibility[48] is the formation of cation vacancies, one for every two incorporated W(VI) ions.[47]

Doping of the anatase TiO_2 matrix with W(VI) ions was further confirmed by Raman spectroscopy (Fig. 3). For bare

Table 1 Experimental composition, specific surface area and anatase lattice parameters for the as synthesized samples

Sample	Nominal and (experimental[a]) WO_3 content in mol%	a axis (Å)	c axis (Å)	Cell volume (Å^3)	Crystallite size (nm)	SSA (m^2 g^{-1})
TiO_2	—	3.7897(7)	9.492(2)	136.33(6)	14	95
WT80	1.2%	3.7890(3)	9.495(1)	136.31(3)	14	103
WT40	2.4% (2.0%)	3.7887(4)	9.488(1)	136.20(4)	12	108
WT20	4.7% (4.0%)	3.7916(3)	9.488(1)	136.41(3)	13	108
WT10	9.0% (8.0%)	3.7976(4)	9.484(1)	136.77(3)	12	117
WT5	17% (18%)	3.8038(3)	9.457(1)	136.83(3)	13	107
WT4	20% (22%)	3.8080(3)	9.445(1)	137.00(3)	13	106
WT3	25% (28%)	3.8102(3)	9.430(1)	136.90(3)	13	93
WT2	33% (29%)	3.8154(4)	9.406(1)	136.93(3)	13	79
WT1	50% (47%)	3.8180(9)	9.402(4)	137.06(9)	9	55
WO_3	—					4

[a] W(VI) contents of the selected samples were determined by XPS and/or EDX.

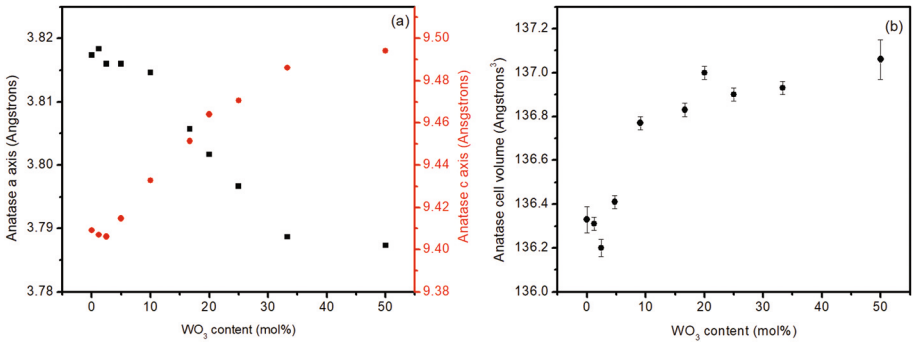

Fig. 2 Variations on the anatase lattice parameters (a) and on the anatase unit cell volume (b) as a function of W(VI) content.

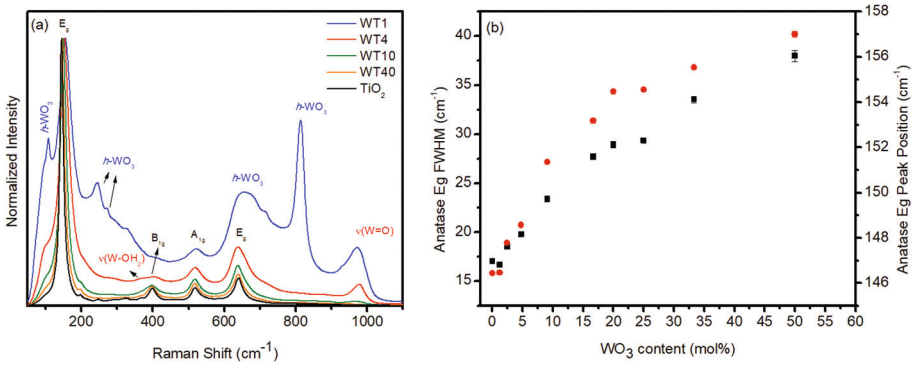

Fig. 3 (a) Raman spectra of bare TiO_2 and selected WT samples. (b) Dependence of E_g peak FWHM (■) and maximum energy (●) on the W(VI) content.

TiO_2, the four most intense peaks of the TiO_2 spectrum at 146, 399, 519 and 640 cm^{-1} could be related to the E_g, B_{1g}, A_{1g} and E_g modes of anatase, respectively. Rutile could also be identified in the spectrum by the small peak at 448 cm^{-1}, as well as brookite, characterized by the weak but distinguishable Raman peaks around 246, 324 and 366 cm^{-1},[49] corroborating with the XRD data. The addition of the W(VI) precursor leads to shifts in the anatase peaks. The peak corresponding to the anatase E_g mode at 146 cm^{-1} was monotonously shifted to higher wavenumbers with increasing W(VI) loading. Moreover, the full widths at half maximum (FWHM) showed the same trend, as shown in Fig. 3b. This behavior confirms the insertion of W(VI) ions in the TiO_2 matrix.

No evidence for crystalline WO_3 was found in the Raman spectra of the TiO_2 rich composites, agreeing with the XRD data. The first occurrence of crystalline WO_3 was observed for WT3 and is ascribed to h-WO_3. As the W(VI) loading is increased in the composites, a broad peak around 970 cm^{-1} is observed and it can be assigned to W═O vibrations,[50] as shown in Fig. 3a. This peak can also be observed in the FTIR spectra of the composites, as shown in Fig. 4, along with an additional peak at 985 cm^{-1}. The intensity of the peak at 985 cm^{-1} increases continuously from WT80 until WT3. For WT1 and WT2, the peak is broadened, probably due to other active modes. W═O vibrations were not observed for bare WO_3 (Fig. S3, ESI†), which exhibits the expected Raman peaks of m-WO_3. The occurrence of terminal W═O cannot be related to crystalline WO_3 and indicates the presence of some amorphous tungsten oxide ($WO_3{\cdot}H_2O$; WO_x) in the composites. A small FTIR peak at ~1620 cm^{-1} could be observed for all samples, except for bare WO_3, and it is assigned to angular vibrations of water molecules. The occurrence of this peak correlated well with a broad band between 3000 and 3600 cm^{-1} (not shown), which belongs to vibrations of the OH bonds in water. Hence, the W–OH and W═O terminations are correlated with the W(VI) doping of anatase TiO_2 and the formation of surface defects.

Electron microscopy studies reveal the distribution of TiO_2 and WO_3 domains in the samples. As revealed by FE-SEM, bare TiO_2 is mainly composed of aggregates of spherical nanoparticles (d < 20 nm, Fig. S4a†), while bare m-WO_3 is composed of much larger plates (Fig. S4b†). Such morphologies correlate well with the N_2 adsorption–desorption isotherms, which revealed that m-WO_3 has very small porosity. Mixed oxides with a low W(VI) content maintained the morphology of bare TiO_2. A representative image for WT4 is shown in Fig. 5a. For high W(VI) loadings, such as WT1, as shown in Fig. 5b, the small TiO_2 particles are decorating the larger WO_3 plates and it is possible to observe larger particles, probably associated with WO_3 domains. HRTEM of the WT4 composite, as shown in Fig. 5c, reveals the presence of anatase TiO_2 particles with ~12 nm diameter. The crystalline TiO_2 particles are intercon-

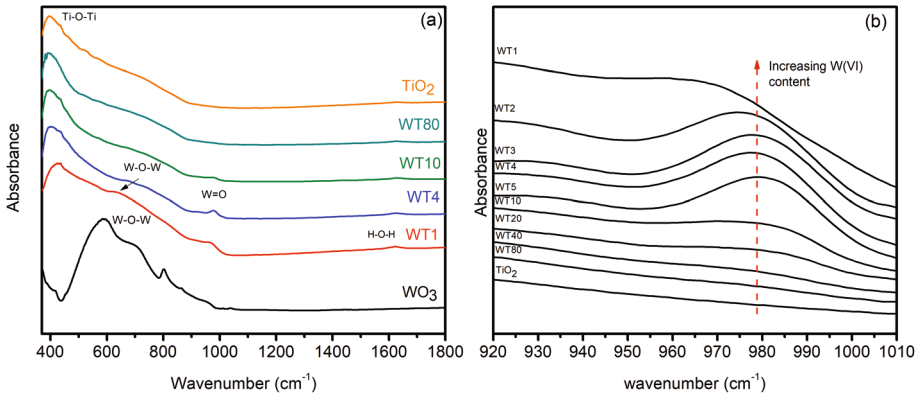

Fig. 4 (a) ATR-IR spectra of representative powder samples. In (b), the spectra in the W═O peak region as a function of W(VI) content are shown.

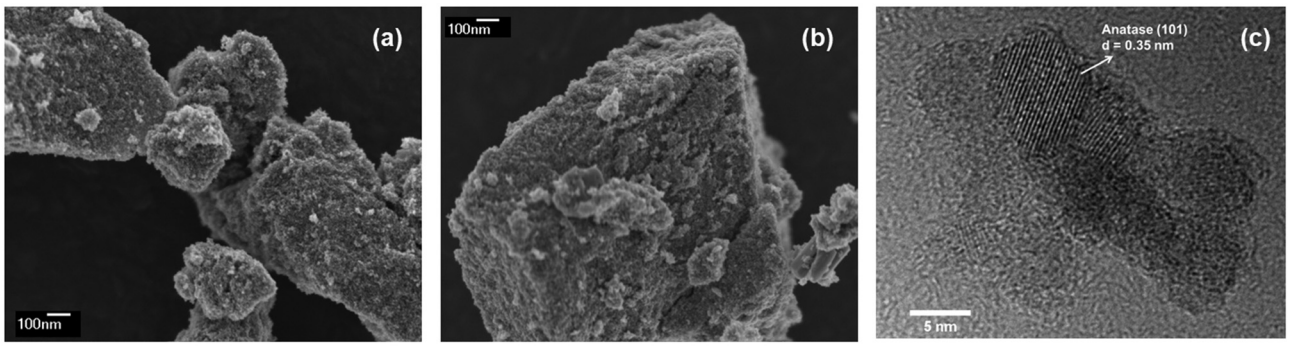

Fig. 5 SEM micrographs of WT4 (a) and WT1(b). (c) High resolution TEM image of WT4.

nected with amorphous WO_3 aggregates, thus confirming the conclusions drawn from vibrational spectroscopy. EDX spectroscopy was carried out for the samples and provided experimental W/Ti ratios, as shown in Table 1. The results are in good agreement with the nominal values. XPS measurements of the selected samples also allow the determination of W/Ti ratios, which agreed well with the values obtained by EDX. A representative XPS spectrum for WT1 is shown in Fig. S5 of ESI.†

UV-vis reflectance spectra of the representative samples are shown in Fig. 6. As expected, bare TiO_2 had an absorption edge at around 420 nm, which corresponds to a band gap energy of 3.0 eV. The absorption edge of bare WO_3 was obviously shifted toward the visible light region due to its smaller band gap (~2.6 eV). Interestingly, the spectra of the Ti rich samples (WT80–WT10) were blue shifted with respect to TiO_2, while the samples with higher W(VI) loadings (WT3–WT1) exhibited absorption tails between those for the bare oxides. The later samples also exhibited a broad absorption feature above 550 nm, which is attributed to the photochromic behavior of these samples after exposure to UV light. The photochromism of WO_3 is well known[51,52] and is attributed to the formation of W(V) sites under illumination, leading to a blue coloration, which is shown in Fig. 6 – inset. These sites are thermodynamically unable to transfer electrons to O_2 in air, and the colors persist for days. The samples WT3–WT1

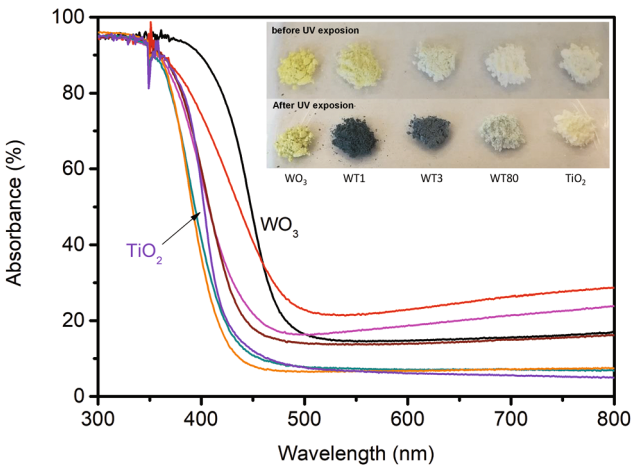

Fig. 6 UV-vis diffuse reflectance spectra of selected photocatalysts: TiO_2(——), WT80 (——), WT20 (——), WT5 (——), WT3 (——), WT1 (——) and WO_3 (—). Inset: Visual observation of the UV-induced photochromic behavior of WT samples.

exhibit the stronger color change compared to the samples with a low W(VI) loading and even more than WO_3. Such a behavior is likely related to the more efficient charge separation due to the presence of a second semiconductor, TiO_2.

Photocatalytic activity

The photocatalytic activities of the TiO_2/WO_3 samples were initially evaluated towards photodegradation of 1 ppm gaseous pollutants (NO and CH_3CHO) using air as the carrier gas. In Fig. 7, the photonic efficiencies determined under UVA irradiation as a function of the photocatalyst composition are shown. Typical plots of the pollutant concentrations as a function of the irradiation time are shown in ESI (Fig. S6†).

Under UVA irradiation, bare TiO_2 and WT80 exhibit the highest photonic efficiencies for acetaldehyde degradation (0.55%, Fig. 7a). As the W(VI) content is increased, the values decreased almost linearly, reaching 0.35% for WT1, which is slightly superior than that for bare WO_3 (ξ = 0.30%). Such a decay of the photocatalytic activity as a function of the W(VI) content is much stronger for NO. Bare TiO_2 has a photonic efficiency of 1.27%. By adding 2 mol% W(VI) (WT80), a decrease of 35% is observed in the photonic efficiency. The values continue to decrease exponentially as the W(VI) content is increased, reaching 0.24% for WT5, which was experimentally similar to the values for WT1 (0.19%) and bare WO_3 (0.16%).

Additional experiments were carried out using pure N_2 as the carrier gas, so the photodegradation occurred under anaerobic conditions. The as-determined photonic efficiencies for bare TiO_2, WT80 and WT40 were 0.37%, 0.35% and 0.34%, respectively. These values are experimentally similar and evidence the role of O_2 as an electron acceptor on the photodegradation mechanism. In bare TiO_2, the electron transfer to O_2 yields reactive peroxide radicals and also diminishes the electron/hole recombination in the semiconductor, improving the degradation rate of the target pollutant. The relative decreases in relation to the photonic efficiencies under aerobic conditions were *ca.* 33% for all samples, which infers that this factor cannot solely explain the variation of the photonic efficiency as a function of the W(VI)/Ti(IV) ratio.

Different from the assays with acetaldehyde that exhibit constant degradation rates over all irradiation times, NO degradation using TiO_2/WO_3 samples exhibits peculiar concentration profiles in relation to the bare oxides. This behavior is exemplified in Fig. S6b (ESI†), and it is different from those observed for bare TiO_2 and WO_3, which exhibit steady-state concentrations of NO and NO_2 minutes after the irradiation starts. The WT samples exhibit greater degradation rates at the beginning of the irradiation which decrease after some time. In the presence of WT80, the concentration of NO initially decreased to the same level of that observed for bare TiO_2, but started to increase over the whole illumination time. Even after 2 h, when the light was turned off, the concentration was not in steady equilibrium. The NO_2 concentration increased in the first 20 min of the irradiation, followed by a decreasing trend.

For WT3, the same behavior is observed, but the photocatalyst deactivation is much faster. This behavior was also observed by Mendoza *et al.*[10] The reasons for such differences are not clear, but they are probably related to the photo-induced adsorption of NO and its oxidation products on the surface of WT samples. The mixed TiO_2/WO_3 samples have higher surface areas than bare WO_3 and also W(VI) ions inserted on the TiO_2 lattices, which can act as Lewis adsorption sites for NO_2 and NO_3^-. Moreover, in WT1 and WT2, WO_3 exhibits the hexagonal crystalline phase, which is well known as a gas sensor due to its more opened structure in relation to m-WO_3.[53]

The photocatalytic activity towards acetaldehyde degradation was also evaluated under 425 nm excitation (Fig. 8). At this wavelength, the absorption coefficient varies considerably as a function of the W(VI) content (Fig. 6). As shown in Fig. 8a, the photonic efficiency for acetaldehyde degradation at 425 nm irradiation was higher for bare WO_3 (ξ = 0.22%). Bare TiO_2 exhibited a photonic efficiency of 0.14%, and WT3 exhibited the highest photonic efficiency (ξ = 0.17%) among the composites. Furthermore, if only the fraction of the absorbed light is considered, an apparent quantum yield (AQY) for 425 nm induced degradation of acetaldehyde can be determined (Fig. 8b). Hence, the quantum yields follow the same trend

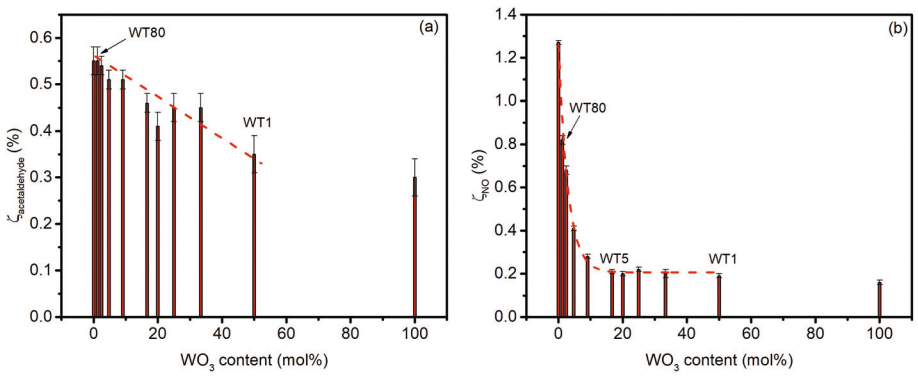

Fig. 7 (a) Photonic efficiencies ζ for acetaldehyde (a) and NO (b) degradation under UV light irradiation (365 nm, 10 W m^{-2}) as a function of the W(VI) content of the samples.

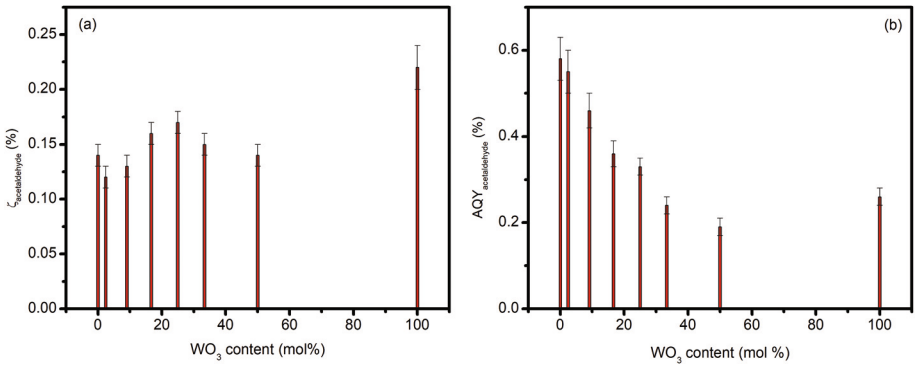

Fig. 8 (a) Photonic efficiencies ζ (a) and apparent quantum yields (b) for acetaldehyde degradation under visible light irradiation (425 nm; 30 W m^{-2}) as a function of the WO_3 content of the samples.

observed for the photonic efficiency under 365 nm irradiation, where the absorbances of the samples are very similar. This result confirms that the charge transfer efficiency between the photocatalyst and acetaldehyde decreases as the W(VI) content increases.

Some samples were also evaluated as photocatalysts for UVA-induced degradation of 2×10^{-5} mol L^{-1} methylene blue aqueous solutions (Fig. 9). Some WT samples were able to adsorb high amounts of MB prior to the beginning of irradiation, which calls particular attention. The sample WT4 removed *ca.* 90% of MB from the solution, while bare WO_3 and TiO_2 removed only 2 and 25%, respectively. After turning on the UV lamp, samples with low W(VI) contents (WT40, WT20) exhibited the highest degradation rates, yielding better photonic efficiencies. For WT40, the as determined photonic efficiency was 0.16%, while for bare TiO_2, values up to 0.06% were found. Bare WO_3 was not active under the same experimental conditions, probably due its very low SSA and its inability to reduce O_2 and produce reactive oxygen species.

The higher photonic efficiency observed for WT40 in relation to those for WT4 and WT1 indicates that the photodegradation of MB following the self-sensitization mechanism is not the main reactive pathway under the experimental conditions employed here (365 nm irradiation). At this excitation wavelength, band gap excitation, followed by interfacial charge transfer, is probably the major degradation pathway.

Transient absorption spectroscopy and photoelectrochemical studies

Aiming at a deeper understanding of the dynamics of the electron/hole pair in photoexcited TiO_2/WO_3 powders and possible interfacial charge transfer processes,[54] nanosecond transient absorption spectroscopy (ns-TAS) studies of selected samples were carried out under N_2 atmosphere and in the presence of methanol vapor. Methanol is well known to act as an efficient hole quencher with the charge transfer occurring at the fs–ps scale.[55] Transient spectra of WT4 and WT1 samples are presented in Fig. 10, while the spectral data for WT10 are shown in Fig. 11. For reference, the ns-TAS spectra of the bare oxides obtained under the same experimental conditions are given in the ESI (Fig. S7, ESI†). The transient spectra of bare TiO_2 exhibit the typical features previously described,[56] *i.e.* a broad absorption band covering basically all the visible region of spectra with the maximum at ~540 nm. This absorption is attributed to the overlap between electronic transitions involving both the trapped holes on the valence band and the

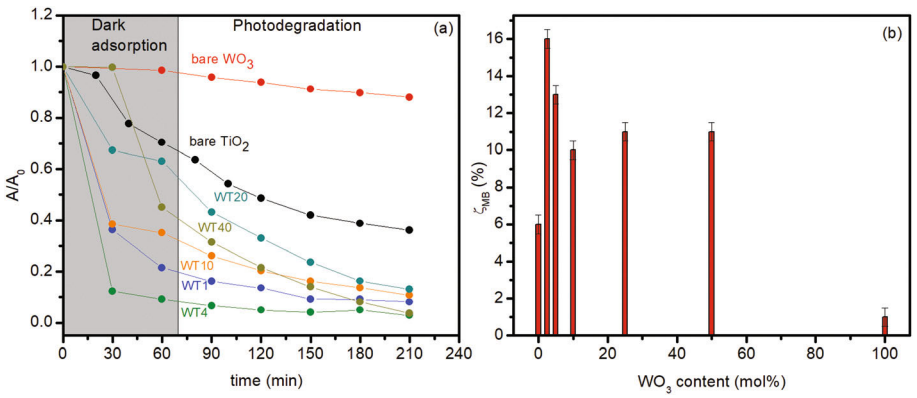

Fig. 9 (a) Relative absorbance variations probed at 660 nm of MB aqueous solutions in the presence of different photocatalysts (T = 298 K). (b) Determined photonic efficiencies for MB photodegradation as a function of W(VI) content in the photocatalysts.

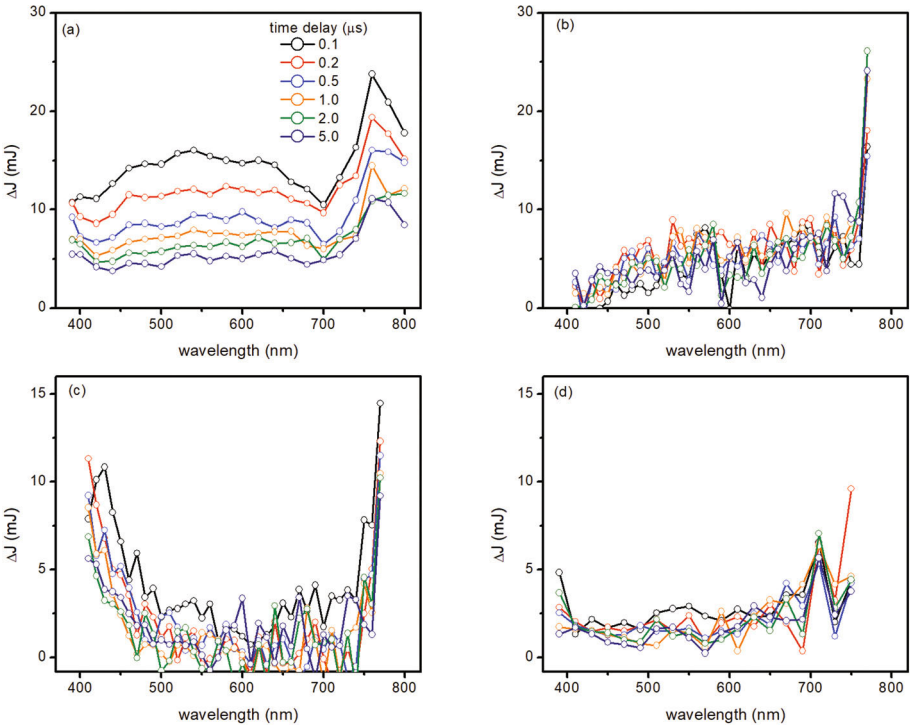

Fig. 10 Transient absorption spectra at different time delays of WT4 (a and b) and WT1 (c and d) samples under N_2 atmosphere (a and c) or in the presence of gaseous methanol (b and d) (355 nm excitation; 3 mJ per pulse).

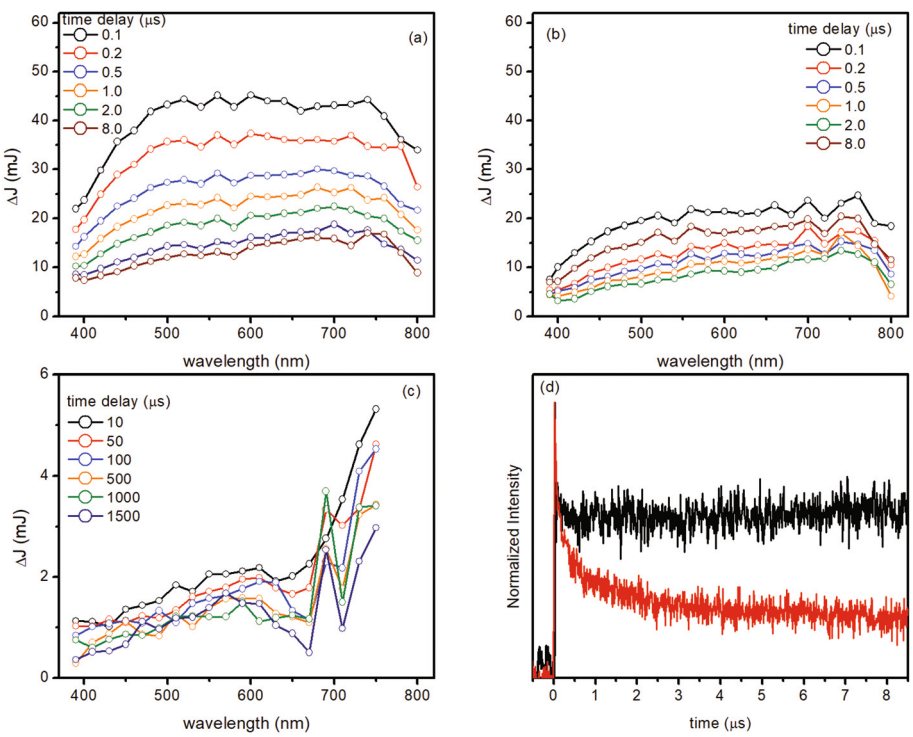

Fig. 11 Transient absorption spectra of WT10 at different time delays after the laser pulse. Measurements performed under N_2 (a) and in the presence of methanol (b and c). (d) Transient decay signal at 540 nm for bare TiO_2 (black) and WT10 (red).

trapped electrons on the conduction band. The transitions associated with the holes are mainly located at lower wavelengths (400–600 nm), while those associated with the trapped electrons are mainly located at higher wavelengths (600–800 nm). This becomes clear when gaseous methanol is added to the medium and reacts with the photogenerated holes (Fig. S8 of ESI†). The transient spectra of bare WO_3 under inert atmosphere are characterized by a strong absorption band with the maximum at ~450 nm (Fig. S7b†), which is mainly attributed to the trapped holes.[12,13] The presence of methanol leads to the same spectral behavior observed for TiO_2, and it is in agreement with previous spectroscopic and spectroelectrochemical studies.[12,13] Under N_2, the transient signals' intensity decays non-exponentially as a result of the electron/hole recombination. This process is hindered in the presence of methanol, and it is not observed up to 8 μs after the laser pulse.

Two different transient spectral profiles could be identified for the WT samples as a function of the W(VI) content at the ns to μs scale after the laser pulse. For W(VI) rich samples (above 10% mol content), the transient spectra under inert atmosphere are basically the sum of the spectral features of the bare oxides. The spectrum of WT4 resembles the spectrum of TiO_2 (Fig. 10a), while the spectral features for WT1 are similar to that for WO_3. For both cases, a strong absorption at longer wavelengths can be observed, which is associated with the blue coloration of the samples under excitation and is ascribed to the formation of W(V) ions in the crystal structure. In the presence of methanol as a hole scavenger, the same behavior as those for the bare oxides is observed, *i.e.* a broad long lived absorption with intensity increasing with the wavelength appears, due to free conduction band electrons. This feature co-exists with the more localized absorption at ~760 nm, assigned to W(V) sites.

A second spectral profile was identified for Ti rich WT samples. As shown in Fig. 11a for WT10, the transient spectrum under N_2 resembles that for bare TiO_2, as expected. However, when methanol is added to the system, the typical signal for free conduction band electrons does not appear immediately (Fig. 11b). In the transient spectrum 200 ns after the laser pulse, ΔJ in the 400–550 nm region is smaller than that collected under N_2, indicating that the hole concentration was decreased, probably due to the fast reaction with methanol. Moreover, the transient signal continues to decay within the first 5 μs, and only at longer time scales, the spectral feature of the free conduction band electrons and the W(V) site can be clearly observed. This is shown in Fig. 11c, in which the signals were collected up to 1.5 ms after the laser pulse. In Fig. 11d, the decay traces at 540 nm of WT10 and TiO_2 in the presence of methanol are shown. Hence, TAS data evidence that the interfacial charge transfer rates of WT samples are actually dependent on the W(VI) content. Particularly for WT samples with up to 10 mol% W(VI) content, it seems the hole transfer to methanol occurs by at least two kinetically distinct pathways: one fraction of photogenerated holes is transferred very fast (below the time resolution of the experiment) to the quencher as observed for the bare oxides, while a second fraction reacts very slowly (at μs scale) or, more likely, even does not react with the quencher and recombines with the trapped electrons.

The transient decays of the different samples under N_2 could be fit as a combination of two second order components, as shown in eqn (3) (Fig. S9, ESI†),[57] assuming that the trapped electrons and holes recombine between themselves. In this equation, ΔJ_2 corresponds to the initial amplitude of the slower component associated with k_2, while k_1 is the rate constant for the fastest component. The determined recombination rate constants, which are shown in Table 2, are expressed in a.u.$^{-1}$ s^{-1} as the conversion of the observed rate constants to units of M^{-1} s^{-1} is difficult due to uncertainties concerning absorption and scattering coefficients of the analyzed materials.

$$\Delta J = \frac{\Delta J_0 - \Delta J_2}{1 + \Delta J_0 k_1 t} + \frac{\Delta J_2}{1 + \Delta J_0 k_2 t} \quad (3)$$

For all bare oxides and WT samples, *ca.* 40% of the trapped holes decay with the fastest rate constant (k_1). Bare WO_3 and W(VI) rich WT samples exhibit lower values of k_1, which agrees well with previous reports in the literature about the long-lived holes on WO_3.[58,59] The same trend is observed for k_2, *i.e.* as the W(VI) content is increased, the recombination rate constant becomes smaller. This is likely due to the electron trapping at long-lived W(V) sites.

Further insights into the dynamics of the photoproduced charge carriers on WT samples were obtained by photoelectrochemical experiments. The samples were deposited on transparent FTO glasses and employed as photoanodes in the presence of aqueous 0.1 mol L^{-1} K_2SO_4 solution and also in the presence of 10 vol% methanol. Chopped light voltammetry measurements of representative photoanodes under simulated solar irradiation are shown in Fig. 12a and b.

For the photoanodes having bare TiO_2 or WO_3, prompt responses to the chopped light were observed in the time–current profiles. In contrast, the WT samples showed saw tooth-shaped curves implying a slower rise and decline of the current densities after turning on and off the light, respectively. In the absence of methanol, the highest photocurrent densities were observed for pure WO_3, as shown in Fig. 12c, which were several magnitudes higher than the photocurrent densities measured for TiO_2 and the composites. The much better performance of bare WO_3 is partially explained by the higher visible light absorption. It is worth mentioning that

Table 2 Second order decay rates obtained for the selected samples under 355 nm excitation (3 mJ per pulse)

Sample	k_1 (10^7 a.u.$^{-1}$ s^{-1})	k_2 (10^5 a.u.$^{-1}$ s^{-1})
TiO_2	1.9 ± 0.1 (43%)	3.4 ± 0.1 (57%)
WT10	1.4 ± 0.1 (43%)	2.9 ± 0.1 (57%)
WT4	1.6 ± 0.1 (44%)	1.5 ± 0.1 (56%)
WT1	0.8 ± 0.1 (40%)	0.9 ± 0.4 (60%)
WO_3	0.36 ± 0.04 (37%)	1.1 ± 0.1 (63%)

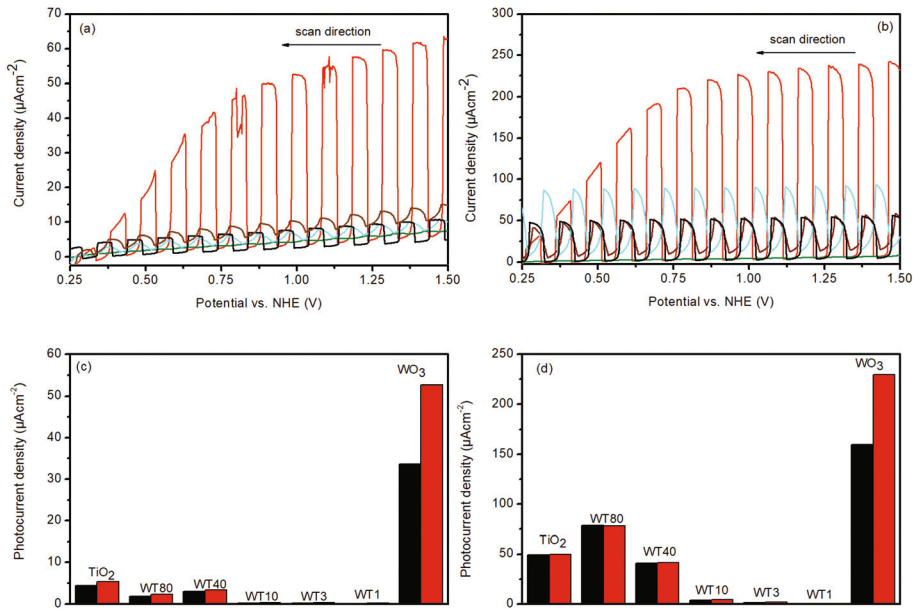

Fig. 12 Chopped light current–potential curves of TiO_2 (—), WT80 (—), WT40 (—), WT1 (—) and WO_3 (—) in the absence (a) and in the presence (b) of methanol. Scan rate of 20 mV s^{-1} upon irradiation with AM 1.5 global light (100 mW cm^{-2}). In (c) and (d) are shown the photocurrent densities for the different semiconductor photoanodes at 0.6 (black) and 1.2 V (red) *vs.* NHE in the absence and presence of methanol, respectively.

TiO_2 and WT40 had better electrochemical performances at the lowest potentials due to earlier photocurrent onsets. Pure TiO_2 showed higher photocurrent densities than all composites. WT1, WT3 and WT10 exhibited almost no current response to the light and consequently extremely low photocurrents. The photocurrent densities in general increased with increasing applied bias. While the Ti rich photoanodes showed very low potential dependency of the photocurrents, the current densities increased much stronger for pure WO_3.

In the presence of 10 vol % methanol, the photocurrent onsets were shifted to more negative potentials for all photoanodes (Fig. 12b). Furthermore, the photocurrent densities were even more constant for the Ti rich electrodes over the whole potential range. WO_3 also showed a strong increase in the photocurrent density with a more positive applied bias. However, unlike water oxidation, the photocurrent density seemed to reach a maximum. Higher photocurrent densities were obtained with methanol for all electrodes, but the relative increments were individually different for all samples. Although WO_3 had the highest photocurrent density, the relative increase was lower compared to TiO_2. Even higher relative increases were found for WT10, WT40 and WT80, resulting in a higher absolute photocurrent density for WT80 than for TiO_2 (Fig. 12d). A general decrease of the photocurrent densities with increasing W(VI) amount in the films could be observed.

Impedance measurements carried out with the electrodes in the 10^6–10^{-1} Hz frequency range and 1 V applied potential (Fig. S10a – ESI†) reveal that the overall impedance of all electrodes is very similar, and no systematic variations could be observed as a function of the film composition. Thus, the different photoelectrochemical performance should be more associated with the interfacial charge transfer at the photoanode/electrolyte interface than with the charge transport properties through the film. Mott–Schottky measurements were also performed with the different electrodes. Plots of C^{-2} *vs.* applied potential (Fig. S10b – ESI†) reveal that all photoanodes strongly deviated from an ideal linear relation, which could be explained by divergences from the ideal behavior of a semiconductor/electrolyte interface. These deviations make it difficult to precisely determine the flat band potentials of the different photoanodes; however, there was an obvious trend towards more positive flatband potentials with increasing W(VI) content. For bare TiO_2, a flatband potential of −0.4 V *vs.* NHE was determined (pH 5.7), which correlated well with the reported values from the literature.[60] For WO_3, the determined flat band potential was −0.08 V *vs.* NHE (pH 5.7).

Discussion

Considering all characterization performed and the photocatalytic assays with different substrates, it is possible to establish the main factors that govern the photocatalytic performance of TiO_2/WO_3 samples. The efficiencies of these photocatalysts are largely dependent on the substrate, the preparation conditions and the W(VI)/Ti(IV) ratio. In fact, reports about both enhanced and worsened photocatalytic activity of TiO_2/WO_3 in relation to bare TiO_2 can be found in the literature. It is well accepted that the formation of a heterojunction between TiO_2 and WO_3 should lead to enhanced charge carrier lifetimes due to the transfer of photoexcited electrons in the TiO_2 to WO_3 conduction band. The TAS measurements under

N_2 have confirmed the decrease of the recombination rate constants.

The conduction band energy edge of crystalline WO_3 is more positive than the one electron reduction of molecular oxygen (E^0 = −0.3 *vs.* NHE, pH = 7); thus, under aerobic conditions and in the absence of another electron acceptor, electrons are accumulated on WO_3, leading to a color change (photochromism). In this case, the photocatalytic activity is hindered as no redox active peroxide species are produced. As a result, TiO_2/WO_3 mixtures with a low W(VI) content (typically between 1–4 mol%) are reported as optimized photocatalysts. Moreover, Yang *et al.* reported that the formation of highly dispersed amorphous WO_x species on the TiO_2 surface is beneficial for photocatalysts as these species have more negative energy levels than crystalline WO_3 and only shallowly trap the photoexcited electrons, allowing the interfacial charge transfer to O_2. The authors observed enhanced photodegradation rates for MB and phenol. On the other hand, Riboni *et al.*[41] suggested that the improved activity observed for 1.0 mol% W(VI)–TiO_2/WO_3 mixed oxides towards formic acid degradation is mainly due to the stabilization of the anatase TiO_2 phase rather than the electron transfer from TiO_2 to WO_3. This stabilization is related to the insertion of W(VI) on the TiO_2 lattice.

The partial replacement of Ti(IV) by W(VI) ions on WT samples has strong consequences on the electronic and surface properties of the powders, which indeed will determine their photocatalytic activity. As evidenced by the N_2 adsorption–desorption isotherms, the specific surface areas of the WT samples up to 25 mol% (WT4) are higher than that for bare TiO_2 likely due to the smaller anatase crystallite size. Moreover, the presence of W(VI) increases the presence of both Brønsted and Lewis adsorption sites on the surface and has a positive effect on the removal of MB from aqueous solutions. As a cationic dye, MB strongly adsorbs on Brønsted sites of WT samples. On the other hand, for NO degradation, surface poisoning of WT photocatalysts is observed in the course of the irradiation, likely due to the Lewis-based interaction of NO_3^- with W(VI) centers.

Insights into the electronic properties of WT samples are first given by the UV-vis spectra. In relation to bare TiO_2, very small spectral changes are observed for the low W(VI) content WT samples (WT80 to WT10). Indeed, the absorption edges of these samples are slightly blue shifted in relation to bare TiO_2, which can be correlated with the smaller particle size. As the W(VI) content exceeds 10 mol%, the absorption edge is shifted to the visible region as expected due to the smaller band gap of WO_3 in relation to TiO_2. UV-induced photochromism confirms the electron transfer from TiO_2 to WO_3, thus evidencing that photogenerated electrons on the TiO_2 conduction band can be efficiently trapped as W(V) sites. ns-transient absorption measurements under inert atmosphere revealed that the electron–hole recombination rates in the WT samples are lower than that for bare TiO_2 and decrease continuously as W(VI) is increased.

Measurements carried out in the presence of methanol, a very efficient hole scavenger, evidenced that a fraction of photogenerated holes in the WT samples does not react with the quencher and recombines at the μs–ms scale with the trapped electrons. This observation was not reported before and should be related to the doping of TiO_2 with W(VI) ions and the formation of amorphous WO_x. Further evidence for the relatively low reactivity of a fraction of trapped holes is given by the very low photocurrent observed for all WT samples with more than 10 mol% in relation to the bare oxides. Even under anodic bias, the interfacial hole transfer in samples having more than 10% WO_3 seems to be kinetically inhibited, resulting in very low photocurrent densities. Previous theoretical studies carried out by Fernandez-Garcia *et al.*[48] indicated that in TiO_2/WO_3, the valence band upper edge energy hardly changes as a function of the W/Ti ratio, but inner states do change due to the stabilizing effect of W(VI) ions on the neighbor oxygens. Thus, deep hole traps could be created.

Therefore, despite the improved charge carrier lifetime in relation to bare TiO_2, the photocatalytic activity of TiO_2/WO_3 samples is limited by inefficient interfacial charge transfer processes: electrons trapped on WO_3 CB are thermodynamically incapable of producing peroxide radicals by one electron oxidation of molecular oxygen, and the reactivity of a fraction of trapped holes is kinetically hindered and actually recombines with the trapped electrons at the μs scale. Both factors become more determinant as the W(VI) content increases. The studies present here could identify two conditions in which the oxidative degradation rates in the presence of TiO_2/WO_3 can overcome that for bare TiO_2. When the photocatalytic assay is carried out under simulated sunlight or even exclusively with irradiation at a given wavelength of the visible region, the red shifted absorption edges of W(VI) WT samples favor the light harvesting and consequently the degradation rates. This was observed for acetaldehyde degradation employing 425 nm LEDs as the light source, in which WT3 (25 mol% W(VI)) exhibited the optimal performance.

Other favorable conditions could be observed for the degradation of aqueous solutions of the cationic methylene blue dye. The species strongly adsorb on WT surfaces and are further degraded under UV irradiation. In this case, WT samples with W(VI) contents between 1 and 2.5% (WT40, WT80) exhibited improved degradation rates. These samples benefit from the larger specific surface area and the stabilization of the anatase phase in relation to bare TiO_2 and should have a larger fraction of reactive electrons and holes in comparison with W(VI) rich samples. The rationalization of the key factors that govern the photocatalytic activity of TiO_2/WO_3 mixed oxides allows the choice of the best photocatalyst composition as a function of the pollutant that will be photooxidized.

Conclusions

The photocatalytic activity of TiO_2/WO_3 mixed oxides was investigated in detail using different gaseous and dissolved

organic targets. The studies corroborate with previous investigations indicating that the more positive conduction band energy of crystalline WO_3 acts as an electron trap, does enhance the electron/hole lifetime, but inhibits the one electron reduction of O_2. The latter aspect seems to prevail as the W(VI) content increases and is detrimental to photocatalysis. Moreover, addition of W(VI) stabilizes the anatase phase of TiO_2 and increases the SSA as well as the concentration of Brønsted and Lewis adsorption sites. This factor has a positive effect on photodegradation of cationic dyes such as MB, but can facilitate surface poisoning by coordinating photoproducts such as NO_3^- in the case of NO degradation. Despite the improved visible light harvesting by WT samples in relation to bare TiO_2, the experiments revealed an additional effect not yet reported for TiO_2/WO_3-based photocatalysts: doping with W(VI) ions seems to induce the formation of deep hole trap states that kinetically inhibit the interfacial charge transfer on the photocatalyst surface. The results provide new insights into how TiO_2/WO_3 with appropriate W/Ti ratios could be chosen as a function of the pollutant to be degraded. Further studies are necessary to identify the nature of the deep hole traps in such systems.

Conflicts of interest

There are no conflicts to declare.

Acknowledgements

This work was supported by Fundação de Amparo à Pesquisa do Estado de Minas Gerais (FAPEMIG, PPM-00220-17), Conselho Nacional de Desenvolvimento Científico e Tecnológico (CNPq) and Coordenação de Aperfeiçoamento de Pessoal de Nível Superior (CAPES). The authors are also thankful to the Grupo de Materiais Inorgânicos do Triângulo (GMIT), a research group supported by FAPEMIG (APQ-00330-14). A. O. T. P. is thankful to Alexander Von Humboldt Foundation for the fellowship in Germany. D. W. B. acknowledges financial support from Saint Petersburg State University (Research Grant 39054581).

References

1 J. Low, J. Yu, M. Jaroniec, S. Wageh and A. A. Al-Ghamdi, Heterojunction Photocatalysts, *Adv. Mater.*, 2017, **29**, 1601694.
2 K. Afroz, M. Moniruddin, N. Bakranov, S. Kudaibergenov and N. Nuraje, A heterojunction strategy to improve the visible light sensitive water splitting performance of photocatalytic materials, *J. Mater. Chem. A*, 2018, **6**, 21696–21718.
3 L. Wei, C. Yu, Q. Zhang, H. Liu and Y. Wang, TiO_2-based heterojunction photocatalysts for photocatalytic reduction of CO_2 into solar fuels, *J. Mater. Chem. A*, 2018, **6**, 22411–22436.
4 N. Fajrina and M. Tahir, A critical review in strategies to improve photocatalytic water splitting towards hydrogen production, *Int. J. Hydrogen Energy*, 2019, **44**, 540–577.
5 A. O. T. Patrocinio, L. F. Paula, R. M. Paniago, J. Freitag and D. W. Bahnemann, Layer-by-Layer TiO_2/WO_3 Thin Films As Efficient Photocatalytic Self-Cleaning Surfaces, *ACS Appl. Mater. Interfaces*, 2014, **6**, 16859–16866.
6 Z. DohĿeviĿ-MitroviĿ, S. StojadinoviĿ, L. Lozzi, S. AškrabiĿ, M. RosiĿ, N. TomiĿ, N. PaunoviĿ, S. LazoviĿ, M. G. NikoliĿ and S. Santucci, WO_3/TiO_2 composite coatings: Structural, optical and photocatalytic properties, *Mater. Res. Bull.*, 2016, **83**, 217–224.
7 A. A. Ismail, I. Abdelfattah, A. Helal, S. A. Al-Sayari, L. Robben and D. W. Bahnemann, Ease synthesis of mesoporous WO_3–TiO_2 nanocomposites with enhanced photocatalytic performance for photodegradation of herbicide imazapyr under visible light and UV illumination, *J. Hazard. Mater.*, 2016, **307**, 43–54.
8 M. Yan, G. Li, C. Guo, W. Guo, D. Ding, S. Zhang and S. Liu, WO_3–x sensitized TiO_2 spheres with full-spectrum-driven photocatalytic activities from UV to near infrared, *Nanoscale*, 2016, **8**, 17828–17835.
9 S. Dominguez, M. Huebra, C. Han, P. Campo, M. N. Nadagouda, M. J. Rivero, I. Ortiz and D. D. Dionysiou, Magnetically recoverable TiO_2-WO_3 photocatalyst to oxidize bisphenol A from model wastewater under simulated solar light, *Environ. Sci. Pollut. Res.*, 2017, **24**, 12589–12598.
10 J. A. Mendoza, D. H. Lee and J.-H. Kang, Photocatalytic removal of gaseous nitrogen oxides using WO_3/TiO_2 particles under visible light irradiation: Effect of surface modification, *Chemosphere*, 2017, **182**, 539–546.
11 C. P. Sajan, A. Naik and H. N. Girish, Hydrothermal fabrication of WO_3-modified TiO_2 crystals and their efficiency in photocatalytic degradation of FCF, *Int. J. Environ. Sci. Technol.*, 2017, **14**, 1513–1524.
12 T. Xu, Y. Wang, X. Zhou, X. Zheng, Q. Xu, Z. Chen, Y. Ren and B. Yan, Fabrication and assembly of two-dimensional $TiO_2/WO_3{\cdot}H_2O$ heterostructures with type II band alignment for enhanced photocatalytic performance, *Appl. Surf. Sci.*, 2017, **403**, 564–571.
13 A. Arce-Sarria, F. Machuca-Martínez, C. Bustillo-Lecompte, A. Hernández-Ramírez and J. Colina-Márquez, Degradation and Loss of Antibacterial Activity of Commercial Amoxicillin with TiO_2/WO_3-Assisted Solar Photocatalysis, *Catalysts*, 2018, **8**, 222.
14 D. S. Han, R. Elshorafa, S. H. Yoon, S. Kim, H. Park and A. Abdel-Wahab, Sunlight-charged heterojunction TiO_2 and WO_3 particle-embedded inorganic membranes for nighttime environmental applications, *Photochem. Photobiol. Sci.*, 2018, **17**, 491–498.
15 K. Huang and Z. Cai, Synthesis of Three-dimensionally Ordered Macroporous TiO_2 and TiO_2/WO_3 Composites and Their Photocatalytic Performance, *Z. Anorg. Allg. Chem.*, 2018, **644**, 1072–1077.
16 H. Khan, M. G. Rigamonti, G. S. Patience and D. C. Boffito, Spray dried TiO_2/WO_3 heterostructure for photocatalytic applications with residual activity in the dark, *Appl. Catal., B*, 2018, **226**, 311–323.

17 J. A. Mendoza, D. H. Lee, L.-H. Kim, I. H. Kim and J.-H. Kang, Photocatalytic performance of TiO_2 and WO_3/TiO_2 nanoparticles coated on urban green infrastructure materials in removing nitrogen oxide, *Int. J. Environ. Sci. Technol.*, 2018, **15**, 581–592.

18 S. Prabhu, L. Cindrella, O. J. Kwon and K. Mohanraju, Photoelectrochemical and photocatalytic activity of TiO_2-WO_3 heterostructures boosted by mutual interaction, *Mater. Sci. Semicond. Process.*, 2018, **88**, 10–19.

19 L. Soares and A. Alves, Photocatalytic properties of TiO_2 and TiO_2/WO_3 films applied as semiconductors in heterogeneous photocatalysis, *Mater. Lett.*, 2018, **211**, 339–342.

20 M. B. Tahir, M. Sagir and K. Shahzad, Removal of acetylsalicylate and methyl-theobromine from aqueous environment using nano-photocatalyst WO_3-TiO_2 @g-C_3N_4 composite, *J. Hazard. Mater.*, 2019, **363**, 205–213.

21 J. Hu, L. Wang, P. Zhang, C. Liang and G. Shao, Construction of solid-state Z-scheme carbon-modified TiO_2/WO_3 nanofibers with enhanced photocatalytic hydrogen production, *J. Power Sources*, 2016, **328**, 28–36.

22 C. Sotelo-Vazquez, R. Quesada-Cabrera, M. Ling, D. O. Scanlon, A. Kafizas, P. K. Thakur, T.-L. Lee, A. Taylor, G. W. Watson, R. G. Palgrave, J. R. Durrant, C. S. Blackman and I. P. Parkin, Evidence and Effect of Photogenerated Charge Transfer for Enhanced Photocatalysis in WO_3/TiO_2 Heterojunction Films: A Computational and Experimental Study, *Adv. Funct. Mater.*, 2017, **27**, 1605413.

23 H. Liu, W. Guo, Y. Li, S. He and C. He, Photocatalytic degradation of sixteen organic dyes by TiO_2/WO_3-coated magnetic nanoparticles under simulated visible light and solar light, *J. Environ. Chem. Eng.*, 2018, **6**, 59–67.

24 H. Tada, A. Kokubu, M. Iwasaki and S. Ito, Deactivation of the TiO_2 Photocatalyst by Coupling with WO_3 and the Electrochemically Assisted High Photocatalytic Activity of WO_3, *Langmuir*, 2004, **20**, 4665–4670.

25 S. Higashimoto, Y. Ushiroda and M. Azuma, Electrochemically Assisted Photocatalysis of Hybrid WO_3/TiO_2 Films: Effect of the WO_3 Structures on Charge Separation Behavior, *Top. Catal.*, 2008, **47**, 148–154.

26 C.-F. Lin, C.-H. Wu and Z.-N. Onn, Degradation of 4-chlorophenol in TiO_2, WO_3, SnO_2, TiO_2/WO_3 and TiO_2/SnO_2 systems, *J. Hazard. Mater.*, 2008, **154**, 1033–1039.

27 J. Yang, X. Zhang, H. Liu, C. Wang, S. Liu, P. Sun, L. Wang and Y. Liu, Heterostructured TiO_2/WO_3 porous microspheres: Preparation, characterization and photocatalytic properties, *Catal. Today*, 2013, **201**, 195–202.

28 L. Yang, Z. Si, D. Weng and Y. Yao, Synthesis, characterization and photocatalytic activity of porous WO_3/TiO_2 hollow microspheres, *Appl. Surf. Sci.*, 2014, **313**, 470–478.

29 G. Žerjav, M. S. Arshad, P. Djinović, J. Zavašnik and A. Pintar, Electron trapping energy states of TiO2–WO3 composites and their influence on photocatalytic degradation of bisphenol A, *Appl. Catal., B*, 2017, **209**, 273–284.

30 A. O. T. Patrocinio, E. B. Paniago, R. M. Paniago and N. Y. M. Iha, XPS characterization of sensitized *n*-TiO_2 thin films for dye-sensitized solar cell applications, *Appl. Surf. Sci.*, 2008, **254**, 1874–1879.

31 A. O. T. Patrocinio, A. El-Bachá, E. B. Paniago, R. M. Paniago and N. Y. M. Iha, Influence of the Sol-Gel pH Process and Compact Film on the Efficiency of TiO_2-Based Dye-Sensitized Solar Cells, *Int. J. Photoenergy*, 2012, **2012**, 7.

32 E. P. Barrett, L. G. Joyner and P. P. Halenda, The Determination of Pore Volume and Area Distributions in Porous Substances. I. Computations from Nitrogen Isotherms, *J. Am. Chem. Soc.*, 1951, **73**, 373–380.

33 A. O. T. Patrocinio, J. Schneider, M. D. Franca, L. M. Santos, B. P. Caixeta, A. E. H. Machado and D. W. Bahnemann, Charge carrier dynamics and photocatalytic behavior of TiO_2 nanopowders submitted to hydrothermal or conventional heat treatment, *RSC Adv.*, 2015, **5**, 70536–70545.

34 K. A. Borges, L. M. Santos, R. M. Paniago, N. M. Barbosa Neto, J. Schneider, D. W. Bahnemann, A. O. T. Patrocinio and A. E. H. Machado, Characterization of a highly efficient N-doped TiO_2 photocatalyst prepared via factorial design, *New J. Chem.*, 2016, **40**, 7846–7855.

35 T.-P. Lin and H. K. A. Kan, Calculation of Reflectance of a Light Diffuser with Nonuniform Absorption, *J. Opt. Soc. Am.*, 1970, **60**, 1252–1256.

36 R. W. Kessler, G. Krabichler, S. Uhl, D. Oelkrug, W. P. Hagan, J. Hyslop and F. Wilkinson, Transient Decay Following Pulse Excitation of Diffuse Scattering Samples, *Optica Acta: Int. J. Optics*, 1983, **30**, 1099–1111.

37 N. O. Balayeva, M. Fleisch and D. W. Bahnemann, Surface-grafted WO_3/TiO_2 photocatalysts: Enhanced visible-light activity towards indoor air purification, *Catal. Today*, 2018, **313**, 63–71.

38 F. Sieland, J. Schneider and D. W. Bahnemann, Photocatalytic activity and charge carrier dynamics of TiO_2 powders with a binary particle size distribution, *Phys. Chem. Chem. Phys.*, 2018, **20**, 8119–8132.

39 J. Tschirch, R. Dillert and D. Bahnemann, Photocatalytic degradation of Methylene blue on fixed powder layers: Which limitations are to be considered?, *J. Adv. Oxid. Technol.*, 2008, **11**, 193–198.

40 A. Mills, An overview of the methylene blue ISO test for assessing the activities of photocatalytic films, *Appl. Catal., B*, 2012, **128**, 144–149.

41 F. Riboni, M. V. Dozzi, M. C. Paganini, E. Giamello and E. Selli, Photocatalytic activity of TiO2-WO3 mixed oxides in formic acid oxidation, *Catal. Today*, 2017, **287**, 176–181.

42 M. R. Mohammadi, D. J. Fray and A. Mohammadi, Sol–gel nanostructured titanium dioxide: Controlling the crystal structure, crystallite size, phase transformation, packing and ordering, *Microporous Mesoporous Mater.*, 2008, **112**, 392–402.

43 D.-S. Kim, J.-H. Yang, S. Balaji, H.-J. Cho, M.-K. Kim, D.-U. Kang, Y. Djaoued and Y.-U. Kwon, Hydrothermal synthesis of anatase nanocrystals with lattice and surface doping tungsten species, *CrystEngComm*, 2009, **11**, 1621–1629.

44 M. Horn, C. Schwebdtfeger and E. Meagher, Refinement of the structure of anatase at several temperatures, *Z. Kristallogr. – Cryst. Mater.*, 1972, **136**, 273–281.

45 R. D. Shannon, Revised effective ionic radii and systematic studies of interatomic distances in halides and chalcogenides, *Acta Crystallogr., Sect. A: Cryst. Phys., Diffr., Theor. Gen. Crystallogr.*, 1976, **32**, 751–767.

46 F. Riboni, L. G. Bettini, D. W. Bahnemann and E. Selli, WO_3–TiO_2 vs. TiO_2 photocatalysts: effect of the W precursor and amount on the photocatalytic activity of mixed oxides, *Catal. Today*, 2013, **209**, 28–34.

47 A. Kubacka, A. Fuerte, A. Martínez-Arias and M. Fernández-García, Nanosized Ti–V mixed oxides: Effect of doping level in the photo-catalytic degradation of toluene using sunlight-type excitation, *Appl. Catal., B*, 2007, **74**, 26–33.

48 M. Fernández-García, A. Martinez-Arias, A. Fuerte and J. Conesa, Nanostructured Ti– W Mixed-Metal Oxides: Structural and Electronic Properties, *J. Phys. Chem. B*, 2005, **109**, 6075–6083.

49 G. Tompsett, G. Bowmaker, R. Cooney, J. Metson, K. Rodgers and J. Seakins, The Raman spectrum of brookite, TiO_2 (PBCA, Z = 8), *J. Raman Spectrosc.*, 1995, **26**, 57–62.

50 A. Gutiérrez-Alejandre, J. Ramírez and G. Busca, A Vibrational and Spectroscopic Study of WO_3/TiO_2–Al_2O_3 Catalyst Precursors, *Langmuir*, 1998, **14**, 630–639.

51 A. I. Gavrilyuk, Aging of the nanosized photochromic WO_3 films and the role of adsorbed water in the photochromism, *Appl. Surf. Sci.*, 2016, **364**, 498–504.

52 Y.-A. Lee, S.-I. Han, H. Rhee and H. Seo, Correlation between excited d-orbital electron lifetime in polaron dynamics and coloration of WO_3 upon ultraviolet exposure, *Appl. Surf. Sci.*, 2018, **440**, 1244–1251.

53 I. M. Szilágyi, S. Saukko, J. Mizsei, A. L. Tóth, J. Madarász and G. Pokol, Gas sensing selectivity of hexagonal and monoclinic WO_3 to H_2S, *Solid State Sci.*, 2010, **12**, 1857–1860.

54 S. Kumar, K. Ojha and A. K. Ganguli, Interfacial Charge Transfer in Photoelectrochemical Processes, *Adv. Mater. Interfaces*, 2017, **4**, 1600981.

55 J. Schneider, M. Matsuoka, M. Takeuchi, J. Zhang, Y. Horiuchi, M. Anpo and D. W. Bahnemann, Understanding TiO_2 Photocatalysis: Mechanisms and Materials, *Chem. Rev.*, 2014, **114**, 9919–9986.

56 A. O. T. Patrocinio, J. Schneider, M. D. França, L. M. Santos, B. P. Caixeta, A. E. H. Machado and D. W. Bahnemann, Charge carrier dynamics and photocatalytic behavior of TiO_2 nanopowders submitted to hydrothermal or conventional heat treatment, *RSC Adv.*, 2015, **5**, 70536–70545.

57 G. M. Hasselmann and G. J. Meyer, Diffusion-Limited Interfacial Electron Transfer with Large Apparent Driving Forces, *J. Phys. Chem. B*, 1999, **103**, 7671–7675.

58 V. Cristino, S. Marinello, A. Molinari, S. Caramori, S. Carli, R. Boaretto, R. Argazzi, L. Meda and C. A. Bignozzi, Some aspects of the charge transfer dynamics in nanostructured WO_3 films, *J. Mater. Chem. A*, 2016, **4**, 2995–3006.

59 S. Corby, L. Francàs, S. Selim, M. Sachs, C. Blackman, A. Kafizas and J. R. Durrant, Water Oxidation and Electron Extraction Kinetics in Nanostructured Tungsten Trioxide Photoanodes, *J. Am. Chem. Soc.*, 2018, **140**, 16168–16177.

60 H. Kisch, *Semiconductor Photocatalysis*, Wiley-VCH, 2015.